ACS APPLIED MATERIALS & INTERFACES

Research Article

www.acsami.org

Synthesis of Multifunctional Electrically Tunable Fluorine-Doped Reduced Graphene Oxide at Low Temperatures

Faisal Shahzad,[†,‡] Shabi Abbas Zaidi,[*,§] and Chong Min Koo[*,†,‡,∥]

[†]Materials Architecturing Research Center, Korea Institute of Science and Technology, 5, Hwarang-ro 14-gil, Seongbuk-gu, Seoul 02792, Republic of Korea

[‡]Nanomaterials Science and Engineering, University of Science and Technology, 217, Gajung-ro, Yuseong-gu, Daejeon 34113, Republic of Korea

[§]Department of Chemistry, Kwangwoon University, 20 Kwangwoon-ro, Nowon-gu, Seoul 01897, Republic of Korea

[∥]KU-KIST Graduate School of Converging Science and Technology, Korea University, Anam-ro 145, Seongbuk-gu, Seoul 02841, Republic of Korea

Supporting Information

ABSTRACT: Doping with heteroatoms is a well-established method to tune the electronic properties and surface chemistry of graphene. Herein, we demonstrate the synthesis of a fluorine-doped reduced graphene oxide (FrGO) at low temperatures that offers multiple opportunities in applied fields. The as-synthesized FrGO product shows a better electrical conductivity of 750 S m^{-1} than that of undoped rGO with an electrical conductivity of 195 S m^{-1}. To demonstrate the multifunctional applications of the as-synthesized FrGO, it was examined for electromagnetic interference shielding and electrochemical sensing of histamine as an important food biomarker. A laminate of FrGO delivered an EMI shielding effectiveness value of 22 dB in Ku band as compared with 11.2 dB for an rGO laminate with similar thickness. On the other hand, an FrGO modified sensor offered an excellent sensitivity (~7 nM), wide detection range, and good selectivity in the presence of similar biomarkers. This performance originates from the better catalytic ability of FrGO as compared with rGO, where fluorine atoms play the role of catalytic active sites owing to their high electronegativity. The fluorination reaction also helps to improve the reduction degree of the chemically synthesized graphene, consequently enhancing the electrical conductivity, which is a prime requirement for increasing the electromagnetic and electrochemical properties of graphene.

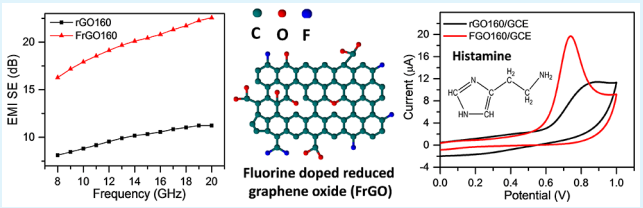

KEYWORDS: *graphene, fluorine doping, electromagnetic interference shielding, biosensor, histamine*

1. INTRODUCTION

Graphene has attracted tremendous attention since its discovery in fundamental and applied research because of its unique 2D honeycomb structure, tunable surface chemistry, high surface area, excellent electronic properties, and chemical stability.[1−4] Because the material properties are related to its chemical structure, many attempts have been made to study the effect of heteroatom dopants (boron, nitrogen, sulfur, phosphorus, fluorine, nitrogen/boron, nitrogen/sulfur, or sulfur/phosphorus) on the electronic and electrochemical properties of graphene.[5−7] For example, B- and N-doped graphene were observed to possess the ability to detect biomolecules, such as ascorbic acid, dopamine, and uric acid.[3,8] Similarly, the S-doped graphene delivered an improved electrical conductivity and in turn the enhanced electromagnetic interference (EMI) shielding and biosensing properties as compared with undoped graphene.[7,9,10] In another report, excellent sensing for NH_3 was achieved using P-doped graphene.[11] Yang and co-workers[5] and Zheng and co-workers[6] observed enhanced synergistic catalysis performances in B- and N-codoped graphene. In all these studies, the increase in catalytic ability of heteroatom-doped graphene was ascribed to the formation of charged sites resulting from difference in electronegativity values between carbon and heteroatom dopants, leading to redistribution of spin and charge densities in graphene.

The fluorine doping process is evolving, and a growing interest exists to study the physicochemical properties of F-doped graphene principally because of the different electronegativity of fluorine and carbon, which may bring interesting features when doped in the graphene lattice.[12,13] Jankovsky and co-workers[14] developed a water-soluble highly fluorinated graphite oxide with tunable fluorescence properties. Jeon and co-workers[15] and Wang and co-workers[16] observed the formation of wide band gap upon fluorination, which is considered enough for photonic and optoelectronic applications in the blue/UV spectrum. Urbanova and co-workers[17] explored the electrochemical behavior and electrocatalytic

Received: April 10, 2017
Accepted: June 27, 2017
Published: June 27, 2017

DOI: 10.1021/acsami.7b05021
ACS Appl. Mater. Interfaces 2017, 9, 24179−24189

performance of various fluorinated graphene for detection of different biomolecules, such as NADH, ascorbic acid, and dopamine. In a separate study, Lee and co-workers[18] showed a 31% increment in tensile strength and 26% increase in EMI of multiwall carbon nanotube (MWCNT)/epoxy composites as the fluorine content was regulated.

Among several of the food markers, histamine (β-imidazolylethylamine) is a heterocyclic primary biogenic amine involved in local immune responses as well as regulating physiological functions in the gut and acting as a neurotransmitter.[19] It is found in all human tissues that regulates several important functions, including the gastrointestinal and circulatory functions, inflammatory reactions, and neural modulation.[20,21] Histamine also appears exogenously in food products formed by decarboxylation of the free amino acid histidine, catalyzed either by endogenous decarboxylases or by uncontrolled microbial action during deterioration and spoilage of the foodstuff.[22] The ingestion of high levels of histamine present in food products usually causes histamine poisoning.[23] The symptoms of histamine poisoning include diarrhea, itching, oral burning sensation, red rash, hypotension, headache, nausea, and vomiting.[24] Owing to the critical effect of histamine, the United States Food and Drug Administration (FDA) has established 50 ppm of histamine as the chemical index for fish spoilage.[25] Based on the assessment of poisoning cases, the guidance levels suggested for histamine content in seafood are: for safe consumption <50 ppm; possibly toxic 50−200 ppm; probably toxic 200−1000 ppm, and toxic and unsafe for human consumption >1000 ppm.[26] As a result, several methods, including high performance liquid chromatography (HPLC),[27] capillary electrochromatography (CEC),[28] and fluorometry,[29] have been reported for detection of histamine. Apart from these useful techniques, electrochemical methods offer a promising alternative because of their simplicity, precision, rapid response, and low cost of instrumentation. Thus, many research works on various types of electrode modifications, such as enzyme-based biosensor[30] and conventional modified electrodes,[21,31−33] have been performed.

The extensive literature review on fluorinated graphene suggests that there has been no investigation in EMI shielding or biomolecules (such as histamine) detection using F-doped graphene. So far, several methods have been used to synthesize F-doped graphene through reaction of graphene oxide (GO) with fluorine-containing gaseous agents, for instance, F_2,[34] XeF_2,[35] SF_6,[36] CF_4,[37] or elemental fluorine,[38] with or without the plasma assistance at high temperatures or in combination with high pressures. Solution processing has also been used for efficient fluorination using chemicals, such as diethylaminosulfur trifluoride,[39] 4-(trifluoromethyl)phenylhydrazine,[40] and HF.[16,41] Unfortunately, most of the gaseous precursors are expensive, toxic, and difficult to handle, which render the mass production of F-doped graphene beyond reach. For this purpose, there is a need to establish a scalable, ecofriendly, and low-temperature process for doping synthesis that provides the potentials for multipurpose applications.

In this work, we developed an ecofriendly and low-temperature procedure to synthesize F-doped graphene samples and successfully examined them in two different important applications, including EMI shielding and electrochemical sensing of histamine. To the best of our knowledge, the use of F-doped reduced GO (FrGO) for any similar applications has not been reported so far. This study validates our earlier reports on doped graphene for enhancement of EMI shielding and electrochemical properties and set to open new avenues for research in related fields.

2. EXPERIMENTAL SECTION

2.1. Materials Preparation. Graphene oxide was prepared using a modified Hummer's method from natural graphite flakes (size larger than 80 μm, Sigma-Aldrich) that we reported in the other papers.[9,10] All the chemicals, including hexafluorophosphoric acid solution, HPF_6 (65 wt % solution in H_2O), sulfuric acid (95%−97%), potassium permanganate (99%), hydrogen peroxide (30%), hydrochloric acid (37%), *N*-methyl-2-pyrrolidone (NMP), and histamine, were purchased from Sigma-Aldrich. The fluorination reaction was performed in a Teflon vessel inside an oil bath. Buffer solutions of 0.1 M PBS with various pH were prepared through dissolving appropriate amounts of sodium phosphate dibasic dihydrate ($Na_2HPO_4{\cdot}2H_2O$), sodium phosphate monobasic monohydrate ($NaH_2PO_4{\cdot}H_2O$), and NaCl in water. The histamine solutions were freshly prepared before examinations through diluting the stock solution with appropriate amounts of PBS buffer.

2.2. Synthesis of F-Doped Graphene. The freeze-dried GO powder was sonicated in NMP at a concentration of 1 mg mL^{-1} for 30 min to get a stable GO dispersion. 200 mL of GO solution was transferred to a Teflon vessel, and 50 mL of HPF_6 solution was slowly added over a period of 10 min to avoid sudden exothermic heating. The mixture was stirred and placed in an oil bath at a preset temperature of 100 or 160 °C for 24 h to get FrGO100 and FrGO160 samples, respectively. Afterward, the as-obtained product was separated from solution through centrifugation at 12 000 rpm for 30 min. The sediment was washed several times with plenty of deionized water and acetone until a clear supernatant was obtained. Samples of FrGO100 and FrGO160 powders were obtained through filtration of the dispersion of fluorinated graphene on a cellulose filter paper followed by vacuum drying at 60 °C for 24 h before any further use. A schematic of the fluorination reaction is shown in Scheme 1.

Scheme 1. Synthesis of Fluorine-Doped Reduced Graphene Oxide

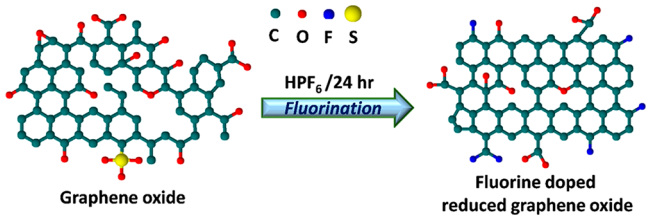

2.3. Synthesis of Reduced Graphene Oxide. A control sample of reduced graphene oxide (rGO) at 160 °C was prepared following a similar procedure except that the fluorinating agent was not added. The as-obtained product was labeled as rGO160.

2.4. Fabrication of Sensors. For the preparation of various types of sensors, first, the surfaces of glassy carbon electrodes (GCEs) were polished and thoroughly rinsed with distilled water. Each GCE surface was electrochemically activated in a 0.01 M H_2SO_4 aqueous solution at a scan rate of 100 mV s^{-1} using 12 times cyclic potential sweeps in the range of −1.0 to 1.0 V. Then, 1−2 μL of freshly prepared (1 mg mL^{-1}) dispersions of rGO160, FrGO100, or FrGO160 in DMF was carefully drop-coated into four successive aliquots onto the sensing area of GCEs and dried for 1 h at ambient temperature to obtain rGO160/GCE, FrGO100/GCE, and FrGO160/GCE sensors. A bare GCE was also used for comparison studies.

2.5. Characterization. A field-emission scanning electron microscope (FE-SEM, Inspect F50, FEI, U.S.A.), equipped with an energy dispersive X-ray spectrometer (EDS) was used for morphological characterization and elemental mapping. TEM (Talos F200X, FEI, USA) was used for EDS elemental mapping, whereas TEM (Titan, FEI, USA) was utilized for HR-TEM images, intensity line profile, and SAED characterizations at an accelerating voltage of 200−300 kV. A

DOI: 10.1021/acsami.7b05021
ACS Appl. Mater. Interfaces 2017, 9, 24179−24189

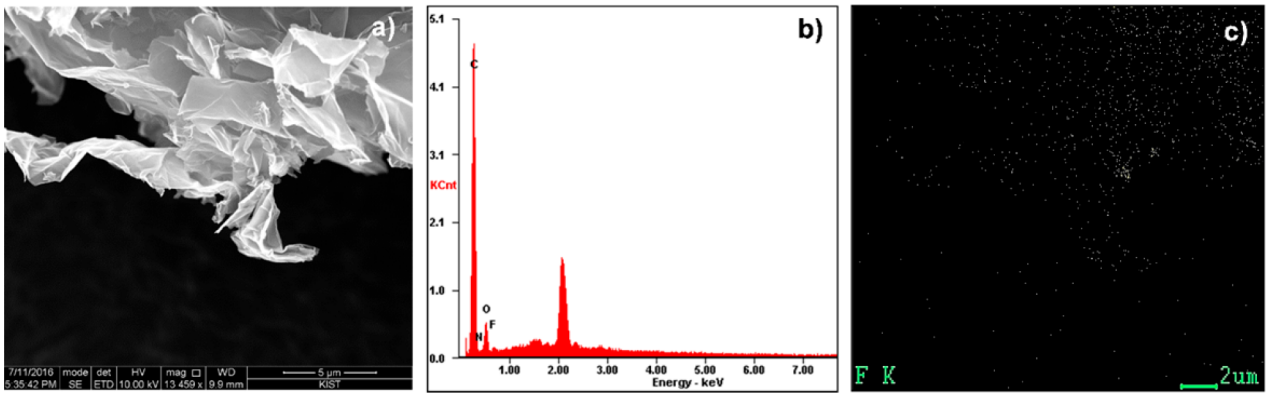

Figure 1. (a) SEM micrograph of FrGO160 flake. (b) EDS spectrum of FrGO160. (c) Fluorine elemental mapping.

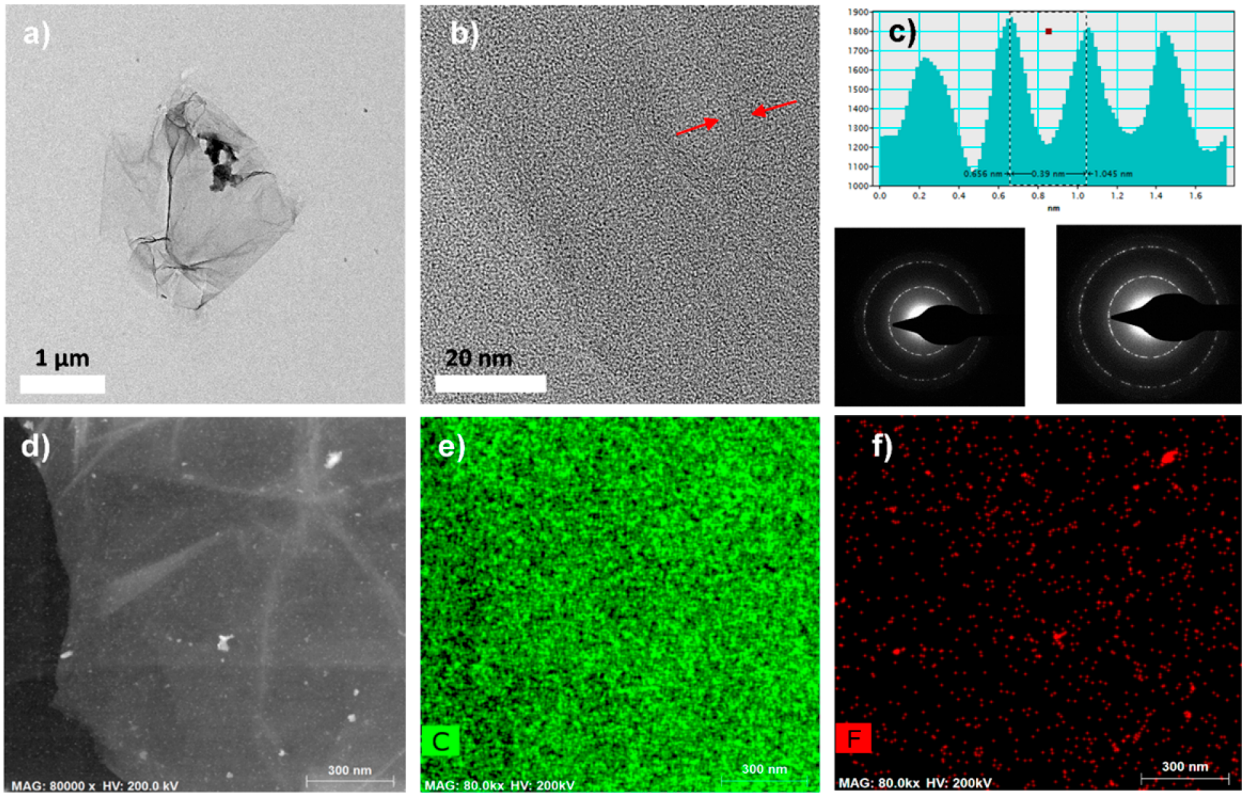

Figure 2. (a) TEM micrograph of FrGO160 sheet. (b) Stacked edges of FrGO160. (c) Thickness profile of selected edge area in (b) and SAED pattern from two different locations. (d–f) TEM micrograph of FrGO160 with corresponding EDS elemental mapping of carbon and fluorine.

drop of diluted colloidal dispersion was placed on a carbon-coated copper grid and allowed to dry in ambient conditions. FT-IR spectra was recorded with a Nicolet iS10 (Thermo Scientific) equipment using the KBR pellet method. The X-ray photoelectron spectroscopy technique (XPS, K-Alpha, Thermo Scientific, U.S.A.) with Al Kα as the X-ray source at a power of 72 W was used to characterize the chemical structures and elemental compositions of doped and undoped samples. Raman spectroscopy was performed using a Raman spectrometer with a 532 nm Ar-ion laser (LabRam HR, Jobin-Yvon, France). Electrical conductivity was measured using a four-pin probe (MCP-TP06P PSP) method with a Loresta GP meter (MCP-T610 model, Mitsubishi Chemical Company, Japan). Thin pellets with a diameter of 10 mm and thickness of 0.5 mm were used for electrical conductivity measurements. For electrochemical measurements and electrochemical impedance spectroscopy (EIS) analysis, a simple three-electrode system was used in which various modified sensors, Pt wire, and Ag/AgCl were applied as a working, counter, and reference electrodes, respectively, in an electrochemical analyzer (Model 600B series, CH Instruments, U.S.A.). For all the experiments, 0.1 M PBS buffer solution (pH 8.0) and scan rate of 100 mV s^{-1} were used unless specified.

3. RESULTS AND DISCUSSION

3.1. Morphology and Chemical Structures. In the microscopic examinations, a typical crumpled sheetlike morphology was observed similar to the common graphene materials in the SEM micrograph of FrGO160 flake (Figure 1). Figure 1b,c shows the corresponding EDS spectra and elemental mapping of fluorine. Figure 2a depicts the TEM micrograph of few layers of FrGO160 graphene sheets deposited on a carbon-coated copper grid. A characteristic crumpled image of transparent F-doped graphene sheets can be observed with wrinkling and edge folding.[16] Figure 2b shows an edge of FrGO160 sheets stacked over one another with

DOI: 10.1021/acsami.7b05021
ACS Appl. Mater. Interfaces 2017, 9, 24179–24189

corresponding intensity line profile in Figure 2c. A *d*-spacing of 0.39 nm was observed in FrGO160 which was slightly larger than *d*-spacing of graphite (0.33 nm). The large *d*-spacing of FrGO160 may be attributed to a repulsive effect from highly electronegative F atoms and other residual oxygenated functional groups that protrude out of the graphene lattice plane.[14] The SAED pattern taken from two different locations show a similar diffused ring pattern indicating a polycrystalline nature of FrGO160 sheets.[42,43] To confirm the F-doping, EDS elemental mapping from a representative TEM image is shown in Figure 2d–f. F atoms were present in the selected scanned area, further substantiating the results from EDS elemental mapping of SEM.

In the Raman spectra of rGO160, FrGO100, and FrGO160 samples (see Supporting Information Figure S1), all the samples exhibited characteristic peaks associated with D and G bands at 1343 and 1583 cm^{-1}, respectively. A slight red-shift of 3–4 cm^{-1} was observed in the D band of FrGO160 as compared with the spectrum of rGO160, presumably owing to the redistribution of electron density in doped graphene as compared with undoped graphene. We also observed an increase in the I_D/I_G ratio from rGO160 (1.02) to FrGO100 (1.09) samples; however, FrGO160 revealed a slight decrease in I_D/I_G ratio (1.05) possibly due to the removal of oxygenated groups and partial restoration of graphitic structure.

Figure 3 shows FT-IR spectra of GO, rGO160, FrGO100, and FrGO160. F-doped samples show two prominent peaks at

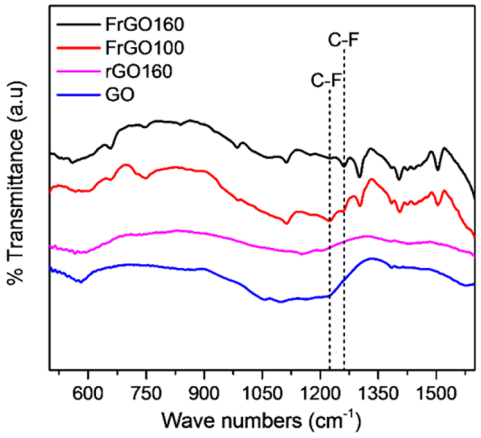

Figure 3. FT-IR spectra of GO, rGO160, FrGO100, and FrGO160.

1261 and 1222 cm^{-1}, resulting from the strong C–F bond stretching which is consistent with the previous reports.[15,44] Full scan XPS spectra of GO, rGO160, FrGO100, and FrGO160 samples were obtained (Figure 4a). In the results, F-doping was confirmed by a characteristic F 1s signals observed nearly at 684.5 eV in FrGO100 and FrGO160 materials validating the findings from FT-IR spectra.[2,40] The C 1s signal was enhanced in FrGO sample, whereas the O 1s peak decreased because of the removal of oxygen-containing functional groups. Figure 4b exhibits the characteristic deconvoluted C 1s spectra of GO with binding energies of 284.6 eV (C=C and C–C), 286.0 eV (–OH, C=OOH, C–O), and 288.8 eV (O–C=O, C=OOH).[10,45] Figure 4c presents the deconvoluted C 1s spectra of FrGO160 at 284.6 eV (C=C and C–C), 285.9 eV(–OH, C–O,C–CF), 287.5 eV (O–C=O), 288.8 eV (C–F), and 291.3 eV (π–π^*).[9,14] A single F 1s peak of FrGO160 with peak center at 686.1 eV was observed in the XPS spectrum of FrGO160 (Figure 4d). The C–F bond was formed as a result of nucleophilic attack of fluorine molecules on the oxygen functional groups such as epoxides and peroxides.[14] The sp^3 C sites in GO enriched with oxygenated groups are an ideal location for chemical attack by fluorine molecules.[16]

The elemental compositions of GO, rGO160, FrGO100, and FrGO160 samples are presented in Table 1. As expected, the fluorine content increased in FrGO160 (1.95 atom %) as compared with FrGO100 (1.25 atom %). The C/O ratio also gradually increased from 2.04 for GO to 7.49 for FrGO material. The larger C/O ratio for FrGO160 sample is possibly due to the better reduction reaction at elevated temperatures (160 °C) in comparison with FrGO100. The rGO, on the contrary, revealed a C/O ratio of 4.37 that depicts insufficient reduction of hydrogenated and other oxygenated groups in similar conditions. It was observed that the fluorinating agent provides not only the necessary fluorine for doping but also assists in reducing the graphene oxide.[2,40]

3.2. Electrical Conductivity and Dielectric Properties. Enhanced reduction of FrGO160 was confirmed through electrical conductivity measurement (Figure 5a). The undoped rGO160 revealed a smaller electrical conductivity value of 195 S m^{-1}, whereas FrGO100 and FrGO160 samples depicted electrical conductivity values of 553 and 750 S m^{-1}, respectively. Thus, these results show about 74% improvement in electrical conductivity of FrGO160 over the undoped rGO prepared at the same temperature. This performance can be attributed to better reduction and removal efficiency of oxygenated groups by fluorinating agent.[2,40]

The complex permittivity variations of rGO160, FrGO100, and FrGO160 samples are plotted in Figure 5b,c as a function of frequency. The complex permittivity values of nanocomposites were calculated using the Nicholson–Ross–Weir method[45] given by eq 1

$$\varepsilon_r = \varepsilon' - j\varepsilon'' \tag{1}$$

where ε' and ε'' represent the dielectric constant (energy storage) and dielectric loss (energy loss), respectively. FrGO160 sample offers ε' value of 110, which is 68% more than that of rGO with ε' value of 38 at 8 GHz. Similarly, FrGO160 provides ε'' value of 77, which is 67% more than that of rGO as 25. The residual oxygen-containing functionalities, such as epoxy, hydroxyl, and carbonyl groups, in rGO act as polarized centers, and are responsible for greater ε' values. The fluorine doping further increases the polarization through providing more scattering centers and differences in local electronegativity around graphene ring. The formation of local dipoles (C–F) and extra scattering centers because of F doping are responsible for enhanced dielectric properties of FrGO160 compared with rGO160.

3.3. EMI Shielding Properties. The EMI shielding effectiveness (SE) of any material can be defined as the logarithm of the ratio of incident power (P_I) to transmitted power (P_T) in decibels[46]

$$SE_T\ (dB) = 10 \log\left(\frac{P_I}{P_T}\right) \tag{2}$$

Generally, EMI shielding occurs by three mechanisms with three distinct effectiveness components: absorption (SE_A), reflection (SE_R), and multiple internal reflections (SE_M). Ohmic losses and energy dissipation in the form of heat within

DOI: 10.1021/acsami.7b05021
ACS Appl. Mater. Interfaces 2017, 9, 24179–24189

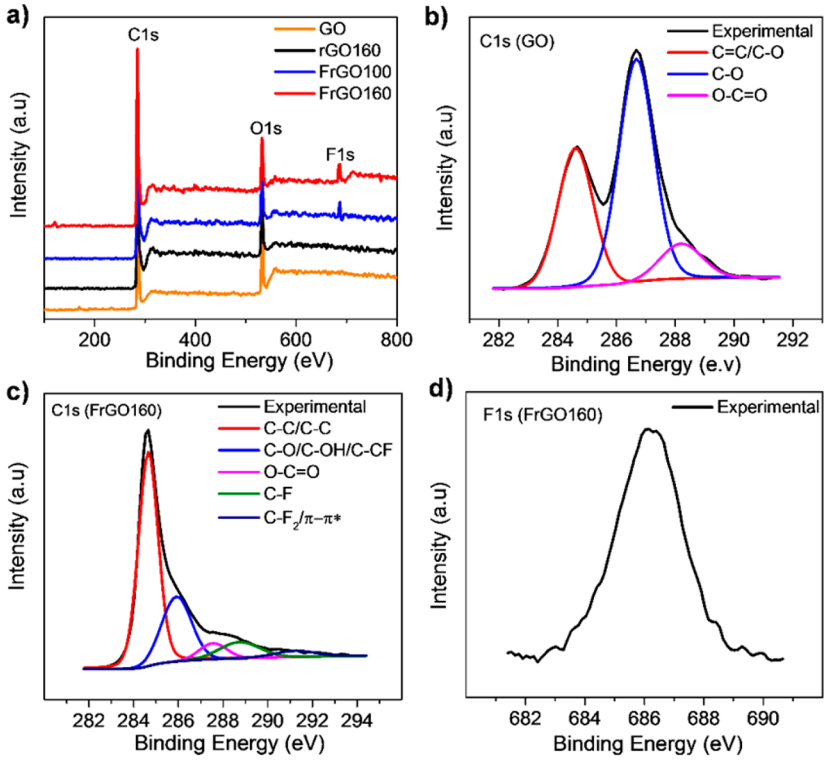

Figure 4. (a) XPS spectra of GO, rGO160, FrGO100, and FrGO160; (b) C 1s spectra of GO; (c) C 1s spectra of FrGO160; and (d) F 1s spectrum of FrGO160.

Table 1. Elemental Composition by XPS Analysis (atom %)

sample	C	O	F	C/O
GO	66.87	32.73	0	2.04
rGO160	81.39	18.61	0	4.37
FrGO100	84.54	14.21	1.25	5.94
FrGO160	86.51	11.54	1.95	7.49

the shielding material occur as a result of absorption mechanism. In contrast, reflection occurs when the EM wave hits a conducting surface and is reflected because of the interactions with the abundant free electrons in the material. The contribution from multiple internal reflections (SE_M) is often ignored when the shielding from absorption is larger than 10 dB, as in that case most of the rereflected waves are absorbed and dissipated as heat within the shielding material.[46] Therefore, SE_T can be expressed in terms of absorption and reflection contributions as eq 3

$$SE_T = SE_A + SE_R \tag{3}$$

Theoretically, SE_A and SE_R can be expressed as[9]

$$SE_A = 8.7d\sqrt{\pi f \mu \sigma} \tag{4}$$

$$SE_R = 39.5 + 10\log\left(\frac{\sigma}{2\pi f \mu}\right) \tag{5}$$

where f is the frequency, σ is the electrical conductivity, μ is the magnetic permeability, and d is the thickness of the shield. According to eqs 4 and 5, EMI SE largely depends on the electrical conductivity and thickness of the shielding materials. Large thickness and electrical conductivity lead to greater EMI shielding values. Experimentally, EMI SE can be measured using a network analyzer that gives the output in the form of scattering parameters (S_{11}, S_{12}, S_{21}, and S_{22}), which are correlated to reflection (R) and transmission coefficients (T) as

$$R = |S_{11}|^2 = |S_{22}|^2, \quad T = |S_{12}|^2 = |S_{21}|^2$$

SE_A and SE_R can be written in terms of scattering parameters as

$$SE_A = 10\log\left(\frac{1-R}{T}\right) = 10\log\left(\frac{1-|S_{11}|^2}{|S_{21}|^2}\right) \tag{6}$$

$$SE_R = 10\log\left(\frac{1}{1-R}\right) = 10\log\left(\frac{1}{1-|S_{11}|^2}\right) \tag{7}$$

Then, eqs 6 and 7 can be solved to deduce SE_T as

$$SE_T = 20\log(S_{21}) \tag{8}$$

The SE_A and SE_R values of rGO160, FrGO100, and FrGO160 samples were determined at various frequencies (Figure 5d,e). Sample FrGO160, the most conductive material among the three samples, showed the greatest EMI value, as expected. Figure 5f summarizes the net EMI SE of the three samples. The larger electrical conductivity results in better shielding owing to strong absorption and reflection of EM waves. The fluorine atoms, which provide a polarizing effect because of difference in electronegativity, also contribute in absorption of the incoming EM waves. Meanwhile, the laminated structure (see Figure S2) provides a multilayered kind of shield where the EM waves, after passing through the first layer, encounter the second layer and so on. The EM waves will encounter several layers before escaping from the other end of the shield. During the process, it is highly likely that the EM waves lose the energy, dissipating in the form of heat.[10,46]

The EMI SE values of different carbon-based materials from the literature are compared in Table 2. The prepared FrGO160

DOI: 10.1021/acsami.7b05021
ACS Appl. Mater. Interfaces 2017, 9, 24179−24189

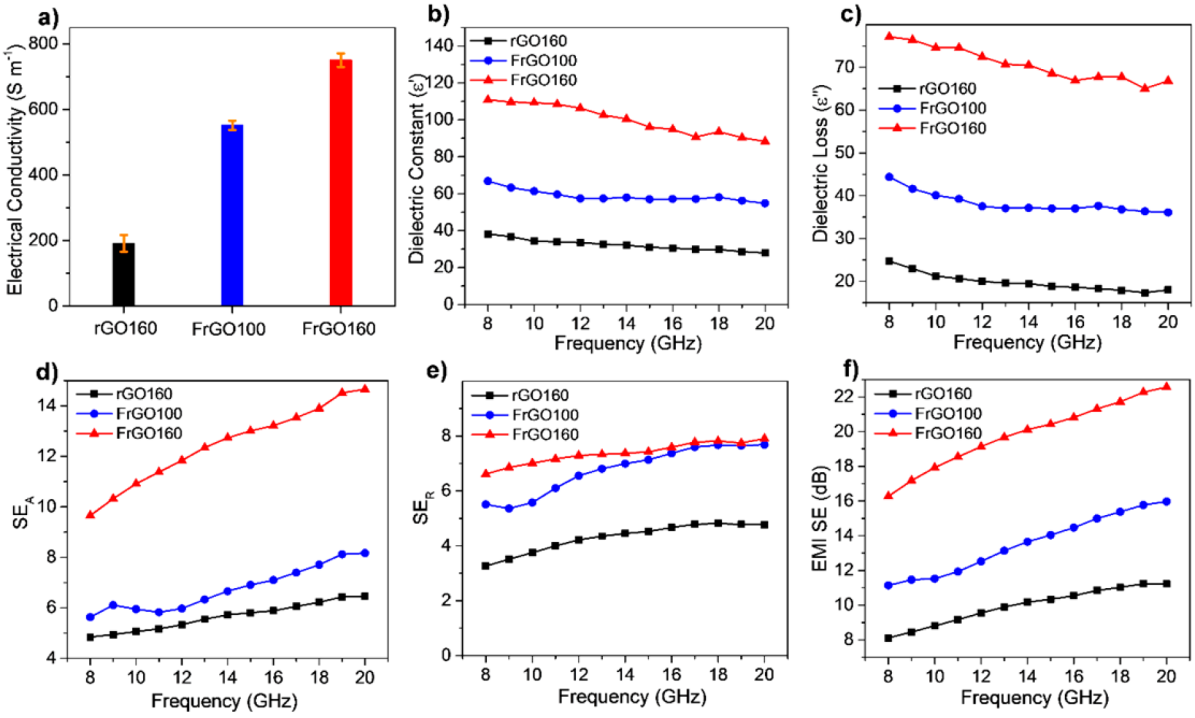

Figure 5. (a) Electrical conductivity values of rGO160, FrGO100, and FrGO160. Variations of (b) dielectric constant and (c) dielectric loss of rGO160, FrGO100, and FrGO160 samples. EMI shielding effectiveness due to (d) absorption, (e) reflection, and (f) total for rGO, FrGO100, and FrGO160 samples.

Table 2. EMI Shielding Performance of Typical Carbon-Based Shielding Materials

filler	matrix	t^a (mm)	σ^b (S m^{-1})	EMI SE (dB)	f^c (GHz)	ref
rGO	PEI[d]	2.3	0.001	22	8.2−12.4	47
rGO/δ-Fe_2O_3	PVA[e]	0.36	3	20.3	8.2−12.4	48
N-doped CNT	PVDF[f]		1700	9.5	0.5−1.5	49
S-doped rGO	PS[g]	2	33	24.5	12.4−18	45
F-doped CNT	epoxy			2.6	0.5−1.5	18
rGO/Fe_3O_4	PEI	2.5	0.0001	18	8.2−12.4	50
CNF/Fe_3O_4	epoxy	13	0.2	20	1−18	51
rGO	PLA[h]	1.5	7.8	17	8.2−12.4	52
rGO/Fe_3O_4	PVA	0.3	<0.1	15	8.2−12.4	53
Ba ferrite	PPY[i]	2	>1	12	2−18	54
GNS	PMMA[j]	2	0.0001	12.2	8.2−12.4	55
CNT/MnOOH	wax	2	17	15	8−18	56
rGO/Fe_3O_4		0.25	5000	21−24	8.2−12.4	57
rGO/Ba ferrite		1	98	18	8.2−12.4	58
GNS		0.25		17	12.4−18	59
F-doped rGO		0.35	750	22.5	8−20	this work

[a]Thickness. [b]Electrical conductivity. [c]Frequency. [d]Poly(ether imide). [e]Poly(vinyl alcohol). [f]Poly(vinylidene fluoride). [g]Polystyrene. [h]Poly(lactic acid). [i]Polypyrrole. [j]Poly(methyl methacrylate).

sample, despite being thin, provide a larger EMI shielding ability as compared with many of the materials reported in the literature. EMI SE can simply be improved through increasing the thickness of the shielding materials. However, use of thick materials causes higher cost and heavier product; thus, it is highly desirable to develop thin shielding materials that can satisfy the minimum shielding requirements above 20 dB in commercial applications.

3.4. Electrochemical Characterization and Analytical Performance of Various Modified Sensors. The electrochemical behavior of the modified sensors was examined using freshly prepared 1 mM $K_3[Fe(CN)_6]^{3-/4-}$ (1:1) solution containing 0.1 M KCl at a scan rate of 100 mV s^{-1} as redox probe with cyclic voltammetry (CV) technique. The results are presented in Figure 6. It is evident from graph in Figure 6a that a well-defined reversible redox couple appears at bare GCE with satisfactory peak separation of about 112 mV. It is worth mentioning here that bare GCE undergoes an activation process when it is being cycled in electrolyte alone. The redox profile shown for bare GCE in the $[Fe(CN)_6]^{3-/4-}$ system corresponds to the first scans that was used for uniform comparison among various electrodes. This observation is consistent with our previous results and other reported ones.[7,60]

DOI: 10.1021/acsami.7b05021
ACS Appl. Mater. Interfaces 2017, 9, 24179−24189

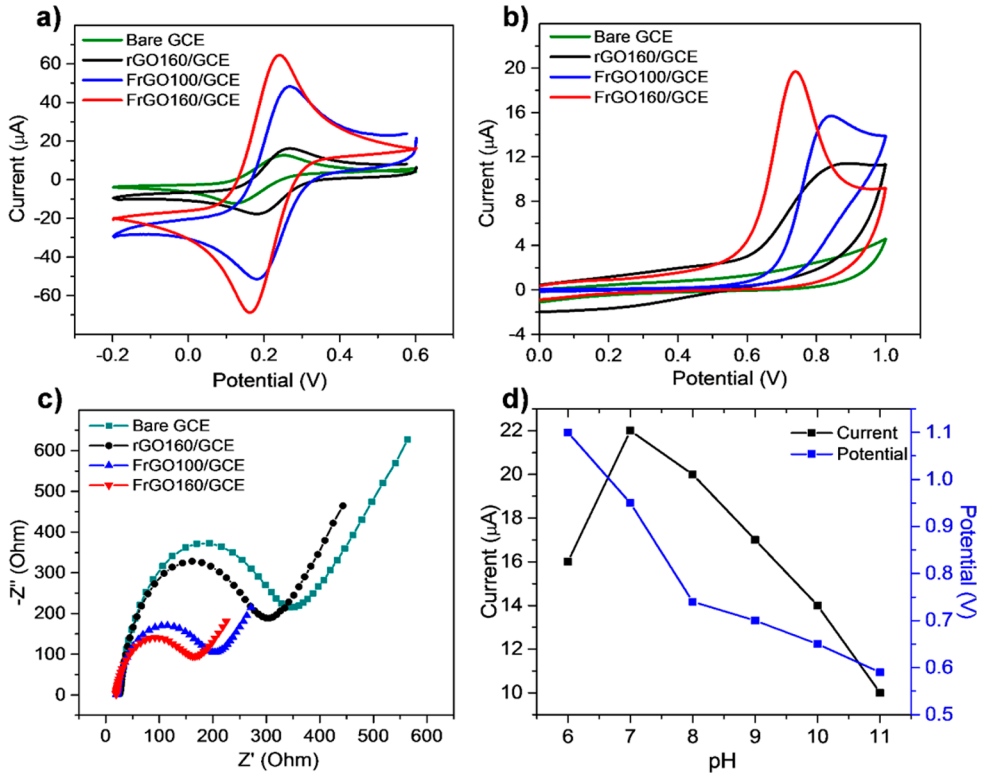

Figure 6. (a) Cyclic voltammograms of bare GCE, rGO/GCE, FrGO100/GCE, and FrGO160/GCE in 1 mM $[Fe(CN)_6]^{3-/4-}$ (1:1) solution containing 0.1 M KCl at scan rate of 100 mV s^{-1}. (b) CV analysis of 4 μM histamine in 0.01 phosphate buffer (pH 8) at scan rate of 100 mV s^{-1}. (c) Nyquist plots of various modified GCE; experimental conditions: 0.1 M PBS (pH 8) with 0.01 M $K_3[Fe(CN)_6]^{3-/4-}$, frequency range of 100 mHz–100 kHz, potential of 0.2 V, ac voltage of 5 mV. (d) Effects of pH on current and peak potential response of 4 μM histamine in 0.01 phosphate buffer at scan rate of 100 mV s^{-1}.

After the modification of electrode with rGO160, the redox peak currents significantly improved with peak-to-peak separation value of approximately 93 mV owing to better electrochemical reversibility of rGO. An explicit redox peak with decreased peak-to-peak separation of nearly 80 mV, and increased peak current signals were obtained with FrGO100/GCE sensor. When the GCE was coated with FrGO160 (FrGO160/GCE), the redox peak current improved further, and the difference between peaks separation decreased to approximately 74 mV. This observation can be attributed to good electrocatalytic ability and increased electrode surface area as a result of gradual increase in fluorine doping, which in turn enhanced the electron conduction from the material surface to the electrode surface. Thus, the FrGO160 sample with the largest fluorine content offered better electron transfer rate compared with FrGO100 as well as with undoped rGO100. The results may be attributed to the increase in the charge transfer properties through the graphene sheets owing to high degree of reduction of GO and surge in defect properties. These observations illustrate a similar behavior as reported in our previous work on sulfur-doped graphene.[7]

Irreversible oxidation peaks were observed with no corresponding reduction peaks in the reverse potential scan of all voltammograms in analysis of histamine with various modified electrode sensors (Figure 6b). In examination with the bare GCE, a relatively poor oxidation peak current was obtained at almost 0.87 V. However, the oxidation peak current of histamine dramatically improved and shifted negatively when using rGO160/GCE sensor. Interestingly, after using FrGO100/GCE and FrGO160/GCE sensors, the oxidation peak current response of histamine greatly increased. As expected, the negative shift in FrGO160 modified sensor is almost 11 mV, which is better than that in FrGO100/GCE sensor. This observation may be attributed to the increase of fluorine content in the FrGO160 sample. The possible nonenzymatic biosensing mechanism of histamine is presented in Scheme 2, showing that histamine is oxidized to 2-(1*H*-imidazol-4-yl)acetonitrile involving identical number of protons and electrons. This result is in close agreement with some previously reported works.[21,32] It is now an established fact that heteroatom doping can alter the energy gap of graphene, which can in turn alter the barrier to electron transfer and therefore the oxidation current response. The decrease in energy gap separation also implies low kinetic stability and high chemical

Scheme 2. Proposed Reaction Mechanism for the Oxidation of Histamine on FrGO160/GCE

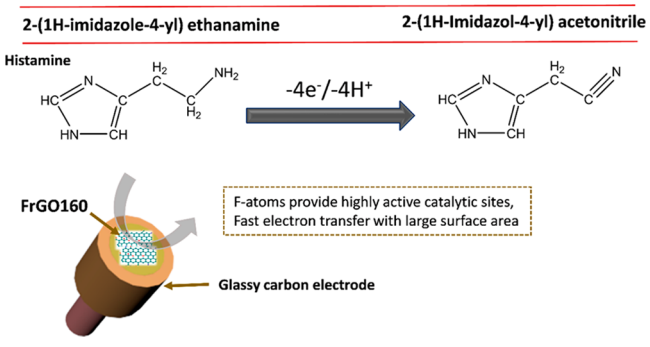

DOI: 10.1021/acsami.7b05021
ACS Appl. Mater. Interfaces 2017, 9, 24179–24189

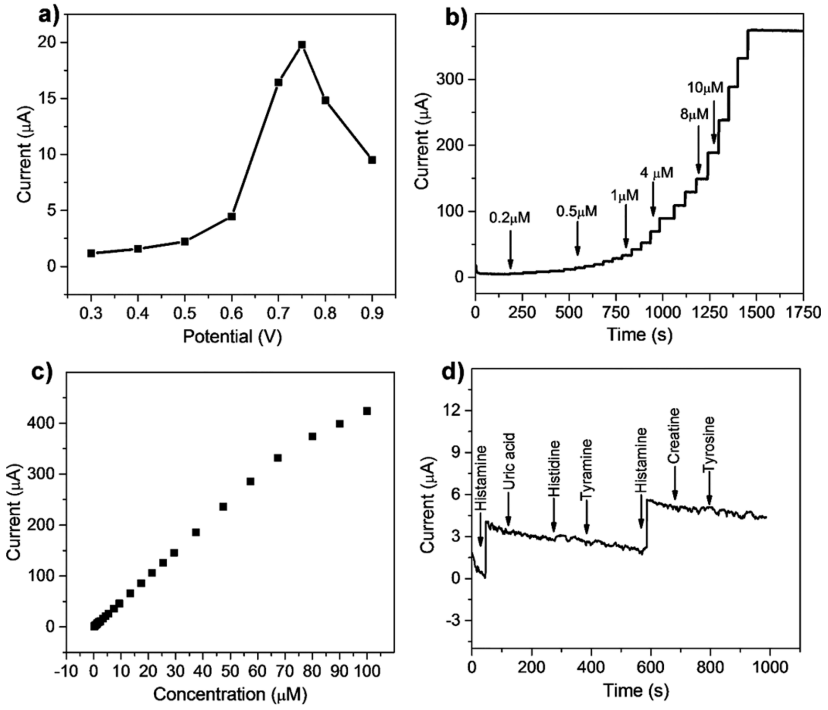

Figure 7. Effects of (a) applied potential, (b) time, and (c) concentration on amperometric current response of 4 μM histamine on FrGO160/GCE sensor. (d) Amperometric $I-T$ curve obtained from FrGO160/GCE sensor for addition of 1 μM histamine and other interfering species (each 8 μM) in 0.01 M PBS (pH 8) at applied potential of 0.74 V.

reactivity because it is energetically favorable to extract electrons from graphene. It has been observed that the signal response of electro-oxidation from histamine increased with the increase in the F doping due to enhanced electron conductivity and creation of C−F bonds. Furthermore, F doping was responsible for more surface defects, and affect the oxidation current response due to altering the barrier to electron transfer. Although, there seems no direct significant role of oxygen-containing groups; however, it has been shown in our previous research works that the number of defects in the doped nanomaterial surface enhances the oxygen adsorption. It is also known that oxidizing behavior of nanomaterial is increased due to increase in the amount of adsorbed oxygen which is responsible for electron emission, thus creating the holes for conduction that play pivotal role in histamine sensing.[61,62] To substantiate the results presented in Figure 6a,b, the electron transfer properties were further characterized with the EIS technique on bare GCE, rGO100/GCE, FrGO100/GCE, and FrGO160/GCE sensors. The charge transfer resistance of R_{ct} was represented by a semicircle in the Nyquist plots (Figure 6c). The Nyquist plots clearly depict that the resistance dramatically decreased in experiment with rGO100/GCE compared with bare GCE material. This observation reveals that modification of GCE with rGO offers lower resistance owing to the fast electron transfer nature of reduced graphene. It also shows further decrease in the value of resistance when using FrGO100/GCE and FrGO160/GCE sensors because of increase in conductivity of the fluorine-doped graphene. The smallest value of impedance was obtained for the electrode modified with graphene containing more fluorine (sample FrGO160). Owing to the high conductivity of the sample FrGO160, one would expect improvement in sensing properties toward histamine; hence, further electrochemical studies were focused only on the FrGO160/GCE sensor.

3.5. Optimization of Experimental Parameters. To achieve the maximum efficiency from as-fabricated FrGO160/GCE sensor, the FrGO160 loading was optimized, as shown in Figure S3. As the graph in Figure S3 illustrates, 1 mg mL^{-1} of graphene and 4 successive drop-coating of sample loading provided the greatest current response; hence, this amount was used to fabricate all the studied sensors. The present graphene loading data matches well with those we previously observed.[7,63]

Valuable information on the behavior of involved electrode processes can be acquired from the relationship between peak current, peak potential, and scan rate. Thus, a scan rate study was conducted for FrGO160/GCE (results shown in Figure S4). A good linear relationship between the square root of the scan rate and the peak current in the range of 20−200 mV s^{-1} with correlation coefficients of 0.997 and 0.995 was observed. This result indicates that the process in the electrodes is diffusion controlled.

The correlations between pH of the supporting electrolyte with the redox behavior of sensor can provide useful information related to oxidation mechanism of histamine. It influences the peak shape and height of a radical formation process, resulting in dimeric structures.[64] Thus, the electrochemical response in 0.1 M phosphate buffer solution with pH in the range of 6.0−11.0 on current and peak potential response of 4 μM histamine at FrGO160/GCE sensor was investigated using the differential pulse voltammetry (DPV) technique. The experimental results shown in Figure 6d demonstrate strong dependency of histamine oxidation in terms of peak potential and peak current on the solution pH. It is evident that the peak potential moves to more negative values with increasing pH; however, the histamine peak current increases with pH increase from 6.0 to 7.0 and then decreases at higher pH until 11.0. Owing to the highest electro-oxidation

DOI: 10.1021/acsami.7b05021
ACS Appl. Mater. Interfaces 2017, 9, 24179−24189

Table 3. Determination of Histamine in Real and Spiked Samples Using FrGO160/GCE Sensor

sample	determined (μM)	added (μM)	expected (μM)	found[a] (μM)	recovery[a] (%)	RSD (%)
cider vinegar	1.5	0.1	1.6	1.54	96.25	3.25
		0.5	2.0	1.95	97.50	2.24
		2.0	3.5	3.53	100.86	3.45
		10.0	11.5	11.20	97.65	2.86
		50.0	51.5	50.90	98.83	4.30
		70.0	71.5	71.80	100.40	2.80

[a] n = 3, mean recovery.

current obtained, accompanied by the best wave manifestation, pH 8.0 was chosen as the most appropriate supporting electrolyte condition for further studies. These results agree with the previously reported ones.[36−39]

3.6. Analytical Performance, Stability, and Reproducibility of Histamine Sensor. The effect of applied potential on the amperometric current response was studied. The current response (Figure 7a) increased as the applied potential shifted from 0.3 V to a more positive value. The maximum current response was observed at 0.746 V. Application of a more positive potential up to 0.9 V decreased the value of current response. Hence, 0.74 V was chosen as the optimum applied potential for histamine detection. A typical current−time response according to the successive addition of various concentrations of histamine at +0.74 V in the buffer solution (pH 8.0) is presented in Figure 7b. Figure 7c shows a linear relationship in the histamine concentration range of 0.2−80 μM with a correlation coefficient of 0.998 using FrGO160/GCE sensor. The detection limit (LOD) was estimated as 7 nM (S/N = 3) with a relative standard deviation (RSD) value of 2.3% based on three measurements.

To investigate the selectivity of the proposed sensor, the amperometric responses to 1 μM histamine and 8 μM of different biological interfering species (such as uric acid, histidine, tyramine, tyrosine, and creatine) were recorded, as shown in Figure 7d. From the amperometric results shown in Figure 7d, it can be inferred that higher concentrations of tyramine, tyrosine, uric acid, and creatine did not affect the histamine peak magnitude because they are not oxidizable under the applied instrumental conditions (applied potential of 0.74 V). On the other hand, there is a minor interference caused by histidine which can be reduced on the lower concentrations of histidine. The obtained results reveal that these compounds do not interfere with histamine detection, indicating that the proposed sensor prevents the diffusion of interfering species even at much larger concentrations.

The analytical applicability of the as-proposed FrGO160/GCE sensor was examined for the determination of histamine after spiking the foodstuff (cider vinegar) obtained from local market. For the analysis, the calculated amount of histamine was separately added to the samples, and recovery of histamine was examined with the help of DPV results. Table 3 summarizes the analytical values obtained for six spiked food samples. The recovery of spiked food samples was in the range from 96.25% to 100.86% with the permissible RSD values. This result indicates the robust and appreciable practicality of the proposed sensor for the detection of histamine in real samples. Furthermore, the reproducibility and stability of the proposed sensor was also examined with three electrodes prepared under the same conditions. The RSD of these three electrodes was determined as 1.6%, 2.2%, and 1.9% for the current responses of histamine, respectively. These results suggest that FrGO160/GCE sensor has a long-time stability as well as good reproducibility and can be used over 2 months without significant change in its response.

4. CONCLUSIONS

We demonstrated a facile strategy to synthesize fluorine-doped graphene using a mild fluorinating agent at relatively low temperatures. Fluorination provides a synergistic effect of improving the electrical conductivity through increasing the reduction degree of reduced graphene oxide and providing local polarization centers that increase the dielectric and EMI shielding properties of reduced graphene oxides. Electrical conductivity and dielectric properties were enhanced by greater than 65% in doped graphene as compared with undoped graphene. Similarly, almost a 100% increment in EMI SE was noted after doping. F-doped graphene samples were also examined for electrochemical detection of histamine. A GCE sensor modified with FrGO160 delivered a robust sensitivity of almost 7 nM, very wide detection window, and an excellent selectivity in the presence of some analogous compounds. This mild approach for fluorine doping is expected to offer promising opportunities to use the F-doped graphene in variety of applications.

■ ASSOCIATED CONTENT

Supporting Information

The Supporting Information is available free of charge on the ACS Publications website at DOI: 10.1021/acsami.7b05021.

SEM micrograph of a FrGO160 laminate, Raman spectra of rGO160, FrGO100, and FrGO160, effect of scan rate on oxidation and reduction potential of FrGO160, and optimizing condition of graphene loading for histamine detection (PDF)

■ AUTHOR INFORMATION

Corresponding Authors

*Tel +82-2-940-8661; Fax +82-29118584; e-mail shabizaidi79@gmail.com (S.A.Z.).

*Tel +8229586872; Fax +8229585309; e-mail koo@kist.re.kr (C.M.K.).

ORCID

Chong Min Koo: 0000-0002-8674-9236

Notes

The authors declare no competing financial interest.

■ ACKNOWLEDGMENTS

This work was supported by Fundamental R&D Program for Core Technology of Materials and the Industrial Strategic Technology Development Program funded by the Ministry of Trade, Industry and Energy, Republic of Korea. This work was

DOI: 10.1021/acsami.7b05021
ACS Appl. Mater. Interfaces 2017, 9, 24179−24189

also partially funded by Korea Institute of Science and Technology through Young Fellow program. The authors are grateful for the support by Basic Science Research Program through the National Research Foundation of Korea (NRF) funded by the Ministry of Science, ICT & Future Planning. S.A.Z. is grateful for research fund in 2017 by Kwangwoon University.

REFERENCES

(1) Usachov, D.; Vilkov, O.; Gruneis, A.; Haberer, D.; Fedorov, A.; Adamchuk, V.; Preobrajenski, A.; Dudin, P.; Barinov, A.; Oehzelt, M. Nitrogen-doped Graphene: Efficient Growth, Structure, and Electronic Properties. *Nano Lett.* **2011**, *11*, 5401−5407.

(2) Qiao, X.; Liao, S.; Wang, G.; Zheng, R.; Song, H.; Li, X. Simultaneous Doping of Nitrogen and Fluorine into Reduced Graphene Oxide: A Highly Active Metal-Free Electrocatalyst for Oxygen Reduction. *Carbon* **2016**, *99*, 272−279.

(3) Sheng, Z.-H.; Zheng, X.-Q.; Xu, J.-Y.; Bao, W.-J.; Wang, F.-B.; Xia, X.-H. Electrochemical Sensor Based on Nitrogen Doped Graphene: Simultaneous Determination of Ascorbic Acid, Dopamine and Uric Acid. *Biosens. Bioelectron.* **2012**, *34*, 125−131.

(4) Tian, Y.; Wei, Z.; Zhang, K.; Peng, S.; Zhang, X.; Liu, W.; Chu, K. Three-Dimensional Phosphorus-Doped Graphene as an Efficient Metal-Free Electrocatalyst for Electrochemical Sensing. *Sens. Actuators, B* **2017**, *241*, 584−591.

(5) Yang, G.-H.; Zhou, Y.-H.; Wu, J.-J.; Cao, J.-T.; Li, L.-L.; Liu, H.-Y.; Zhu, J.-J. Microwave-Assisted Synthesis of Nitrogen and Boron Co-Doped Graphene and its Application for Enhanced Electrochemical Detection of Hydrogen Peroxide. *RSC Adv.* **2013**, *3*, 22597−22604.

(6) Zheng, Y.; Jiao, Y.; Ge, L.; Jaroniec, M.; Qiao, S. Z. Two-Step Boron and Nitrogen Doping in Graphene for Enhanced Synergistic Catalysis. *Angew. Chem.* **2013**, *125*, 3192−3198.

(7) Shahzad, F.; Zaidi, S. A.; Koo, C. M. Highly Sensitive Electrochemical Sensor Based on Environmentally Friendly Biomass-Derived Sulfur-Doped Graphene for Cancer Biomarker Detection. *Sens. Actuators, B* **2017**, *241*, 716−724.

(8) Yeh, M.-H.; Li, Y.-S.; Chen, G.-L.; Lin, L.-Y.; Li, T.-J.; Chuang, H.-M.; Hsieh, C.-Y.; Lo, S.-C.; Chiang, W.-H.; Ho, K.-C. Facile Synthesis of Boron-doped Graphene Nanosheets with Hierarchical Microstructure at Atmosphere Pressure for Metal-free Electrochemical Detection of Hydrogen Peroxide. *Electrochim. Acta* **2015**, *172*, 52−60.

(9) Shahzad, F.; Kumar, P.; Kim, Y.-H.; Hong, S. M.; Koo, C. M. Biomass-Derived Thermally Annealed Interconnected Sulfur-Doped Graphene as a Shield against Electromagnetic Interference. *ACS Appl. Mater. Interfaces* **2016**, *8*, 9361−9369.

(10) Shahzad, F.; Kumar, P.; Yu, S.; Lee, S.; Kim, Y.-H.; Hong, S. M.; Koo, C. M. Sulfur-Doped Graphene Laminates for EMI Shielding Applications. *J. Mater. Chem. C* **2015**, *3*, 9802−9810.

(11) Niu, F.; Tao, L.-M.; Deng, Y.-C.; Wang, Q.-H.; Song, W.-G. Phosphorus Doped Graphene Nanosheets for Room Temperature NH_3 Sensing. *New J. Chem.* **2014**, *38*, 2269−2272.

(12) Tang, S.; Zhang, S. Structural and Electronic Properties of Hybrid Fluorographene−Graphene Nanoribbons: Insight from First-Principles Calculations. *J. Phys. Chem. C* **2011**, *115*, 16644−16651.

(13) Tang, S.; Cao, X. Realizing Semiconductor−Half-Metal Transition in Zigzag Graphene Nanoribbons Supported on Hybrid Fluorographene−Graphane Nanoribbons. *Phys. Chem. Chem. Phys.* **2014**, *16*, 23214−23223.

(14) Jankovský, O.; Šimek, P.; Sedmidubský, D.; Matějková, S.; Janoušek, Z.; Šembera, F.; Pumera, M.; Sofer, Z. Water-Soluble Highly Fluorinated Graphite Oxide. *RSC Adv.* **2014**, *4*, 1378−1387.

(15) Jeon, K.-J.; Lee, Z.; Pollak, E.; Moreschini, L.; Bostwick, A.; Park, C.-M.; Mendelsberg, R.; Radmilovic, V.; Kostecki, R.; Richardson, T. J. Fluorographene: A Wide Bandgap Semiconductor with Ultraviolet Luminescence. *ACS Nano* **2011**, *5*, 1042−1046.

(16) Wang, Z.; Wang, J.; Li, Z.; Gong, P.; Liu, X.; Zhang, L.; Ren, J.; Wang, H.; Yang, S. Synthesis of Fluorinated Graphene with Tunable Degree of Fluorination. *Carbon* **2012**, *50*, 5403−5410.

(17) Urbanová, V.; Karlický, F.; Matěj, A.; Šembera, F.; Janoušek, Z.; Perman, J. A.; Ranc, V.; Čépe, K.; Michl, J.; Otyepka, M. Fluorinated Graphenes as Advanced Biosensors−Effect of Fluorine Coverage on Electron Transfer Properties and Adsorption of Biomolecules. *Nanoscale* **2016**, *8*, 12134−12142.

(18) Lee, S.-E.; Lee, M. Y.; Lee, M.-K.; Jeong, E.; Lee, Y.-S. Effect of Fluorination on the Mechanical Behavior and Electromagnetic Interference Shielding of MWCNT/Epoxy Composites. *Appl. Surf. Sci.* **2016**, *369*, 189−195.

(19) Jutel, M.; Watanabe, T.; Akdis, M.; Blaser, K.; Akdis, C. A. Immune Regulation by Histamine. *Curr. Opin. Immunol.* **2002**, *14*, 735−740.

(20) Yamamoto, K.; Takagi, K.; Kano, K.; Ikeda, T. Bioelectrocatalytic Detection of Histamine Using Quinohemoprotein Amine Dehydrogenase and the Native Electron Acceptor Cytochrome c-550. *Electroanalysis* **2001**, *13*, 375−379.

(21) Švarc-Gajić, J.; Stojanović, Z. Electrocatalytic Determination of Histamine on a Nickel-Film Glassy Carbon Electrode. *Electroanalysis* **2010**, *22*, 2931−2939.

(22) Sarada, B.; Rao, T. N.; Tryk, D.; Fujishima, A. Electrochemical Oxidation of Histamine and Serotonin at Highly Boron-Doped Diamond Electrodes. *Anal. Chem.* **2000**, *72*, 1632−1638.

(23) Taylor, S. L.; Eitenmiller, R. R. Histamine Food Poisoning: Toxicology and Clinical Aspects. *Crit. Rev. Toxicol.* **1986**, *17*, 91−128.

(24) Lehane, L.; Olley, J. Histamine Fish Poisoning Revisited. *Int. J. Food Microbiol.* **2000**, *58*, 1−37.

(25) Grant, F. S. Fish and Fishery Products Hazards and Controls Guidance. *Center for Food Safety and Applied Nutrition* **2011**, *240*, 402−2300.

(26) Keow, C. M.; Bakar, F. A.; Salleh, A. B.; Heng, L. Y.; Wagiran, R.; Bean, L. S. An Amperometric Biosensor for the Rapid Assessment of Histamine Level in Tiger Prawn (Penaeus Monodon) Spoilage. *Food Chem.* **2007**, *105*, 1636−1641.

(27) Dadáková, E.; Pelikánová, T.; Kalač, P. Content of Biogenic Amines and Polyamines in some Species of European Wild-Growing Edible Mushrooms. *Eur. Food Res. Technol.* **2009**, *230*, 163.

(28) Zaidi, S. A. Dual-Templates Molecularly Imprinted Monolithic Columns for the Evaluation of Serotonin and Histamine in CEC. *Electrophoresis* **2013**, *34*, 1375−1382.

(29) Larionova, D.; Shtykov, S.; Beloglazova, N.; Koroleva, E. Effect of Nucleophilic Agents and Organized Media on the Fluorometric Determination of Histamine with O-Phthalic Aldehyde. *J. Anal. Chem.* **2008**, *63*, 1044−1050.

(30) Alonso-Lomillo, M. A.; Domínguez-Renedo, O.; Matos, P.; Arcos-Martínez, M. J. Disposable Biosensors for Determination of Biogenic Amines. *Anal. Chim. Acta* **2010**, *665*, 26−31.

(31) Carralero, V.; González-Cortés, A.; Yáñez-Sedeño, P.; Pingarron, J. Pulsed Amperometric Detection of Histamine at Glassy Carbon Electrodes Modified with Gold Nanoparticles. *Electroanalysis* **2005**, *17*, 289−297.

(32) Stojanović, Z. S.; Mehmeti, E.; Kalcher, K.; Guzsvány, V.; Stanković, D. M. SWCNT-Modified Carbon Paste Electrode as an Electrochemical Sensor for Histamine Determination in Alcoholic Beverages. *Food. Anal. Methods.* **2016**, *9*, 2701−2710.

(33) Geto, A.; Tessema, M.; Admassie, S. Determination of Histamine in Fish Muscle at Multi-Walled Carbon Nanotubes Coated Conducting Polymer Modified Glassy Carbon Electrode. *Synth. Met.* **2014**, *191*, 135−140.

(34) Walter, A. L.; Jeon, K.-J.; Bostwick, A.; Speck, F.; Ostler, M.; Seyller, T.; Moreschini, L.; Kim, Y. S.; Chang, Y. J.; Horn, K.; Rotenberg, E. Highly p-Doped Epitaxial Graphene Obtained by Fluorine Intercalation. *Appl. Phys. Lett.* **2011**, *98*, 184102.

(35) Lee, W.-K.; Robinson, J. T.; Gunlycke, D.; Stine, R. R.; Tamanaha, C. R.; King, W. P.; Sheehan, P. E. Chemically Isolated Graphene Nanoribbons Reversibly Formed in Fluorographene Using Polymer Nanowire Masks. *Nano Lett.* **2011**, *11*, 5461−5464.

(36) Yang, H.; Chen, M.; Zhou, H.; Qiu, C.; Hu, L.; Yu, F.; Chu, W.; Sun, S.; Sun, L. Preferential and Reversible Fluorination of Monolayer Graphene. *J. Phys. Chem. C* **2011**, *115*, 16844−16848.

DOI: 10.1021/acsami.7b05021
ACS Appl. Mater. Interfaces 2017, 9, 24179−24189

(37) Yu, X.; Lin, K.; Qiu, K.; Cai, H.; Li, X.; Liu, J.; Pan, N.; Fu, S.; Luo, Y.; Wang, X. Increased Chemical Enhancement of Raman Spectra for Molecules Adsorbed on Fluorinated Reduced Graphene Oxide. *Carbon* **2012**, *50*, 4512−4517.
(38) Tahara, K.; Iwasaki, T.; Matsutani, A.; Hatano, M. Effect of Radical Fluorination on Mono- and Bi-Layer Graphene in Ar/F_2 Plasma. *Appl. Phys. Lett.* **2012**, *101*, 163105.
(39) Zhao, F.-G.; Zhao, G.; Liu, X.-H.; Ge, C.-W.; Wang, J.-T.; Li, B.-L.; Wang, Q.-G.; Li, W.-S.; Chen, Q.-Y. Fluorinated Graphene: Facile Solution Preparation and Tailorable Properties by Fluorine-Content Tuning. *J. Mater. Chem. A* **2014**, *2*, 8782−8789.
(40) Kim, S.-H.; Lee, C.-H.; Yun, J.-M.; Noh, Y.-J.; Kim, S.-S.; Lee, S.; Jo, S. M.; Joh, H.-I.; Na, S.-I. Fluorine-Functionalized and Simultaneously Reduced Graphene Oxide as a Novel Hole Transporting Layer for Highly Efficient and Stable Organic Photovoltaic Cells. *Nanoscale* **2014**, *6*, 7183−7187.
(41) Yang, X.; Jia, X.; Ji, X. Acid Induced Fluorinated Graphene Oxide. *RSC Adv.* **2015**, *5*, 9337−9340.
(42) Thiruppathi, A. R.; Sidhureddy, B.; Keeler, W.; Chen, A. Facile One-Pot Synthesis of Fluorinated Graphene Oxide for Electrochemical Sensing of Heavy Metal Ions. *Electrochem. Commun.* **2017**, *76*, 42−46.
(43) Ren, M.; Wang, X.; Dong, C.; Li, B.; Liu, Y.; Chen, T.; Wu, P.; Cheng, Z.; Liu, X. Reduction and Transformation of Fluorinated Graphene Induced by Ultraviolet Irradiation. *Phys. Chem. Chem. Phys.* **2015**, *17*, 24056−24062.
(44) Wang, X.; Wang, W.; Liu, Y.; Ren, M.; Xiao, H.; Liu, X. Characterization of Conformation and Locations of C−F Bonds in Graphene Derivative by Polarized ATR-FTIR. *Anal. Chem.* **2016**, *88*, 3926−3934.
(45) Shahzad, F.; Yu, S.; Kumar, P.; Lee, J.-W.; Kim, Y.-H.; Hong, S. M.; Koo, C. M. Sulfur Doped Graphene/Polystyrene Nanocomposites for Electromagnetic Interference Shielding. *Compos. Struct.* **2015**, *133*, 1267−1275.
(46) Shahzad, F.; Alhabeb, M.; Hatter, C. B.; Anasori, B.; Hong, S. M.; Koo, C. M.; Gogotsi, Y. Electromagnetic Interference Shielding with 2D Transition Metal Carbides (MXenes). *Science* **2016**, *353*, 1137−1140.
(47) Ling, J.; Zhai, W.; Feng, W.; Shen, B.; Zhang, J.; Zheng, W. g. Facile Preparation of Lightweight Microcellular Polyetherimide/Graphene Composite Foams for Electromagnetic Interference Shielding. *ACS Appl. Mater. Interfaces* **2013**, *5*, 2677−2684.
(48) Yuan, B.; Bao, C.; Qian, X.; Song, L.; Tai, Q.; Liew, K. M.; Hu, Y. Design of Artificial Nacre-Like Hybrid Films as Shielding to Mitigate Electromagnetic Pollution. *Carbon* **2014**, *75*, 178−189.
(49) Arjmand, M.; Chizari, K.; Krause, B.; Pötschke, P.; Sundararaj, U. Effect of Synthesis Catalyst on Structure OF Nitrogen-Doped Carbon Nanotubes and Electrical Conductivity and Electromagnetic Interference Shielding of their Polymeric Nanocomposites. *Carbon* **2016**, *98*, 358−372.
(50) Shen, B.; Zhai, W.; Tao, M.; Ling, J.; Zheng, W. Lightweight, Multifunctional Polyetherimide/Graphene@Fe_3O_4 Composite Foams for Shielding of Electromagnetic Pollution. *ACS Appl. Mater. Interfaces* **2013**, *5*, 11383−11391.
(51) Crespo, M.; Méndez, N.; González, M.; Baselga, J.; Pozuelo, J. Synergistic Effect of Magnetite Nanoparticles and Carbon Nanofibres in Electromagnetic Absorbing Composites. *Carbon* **2014**, *74*, 63−72.
(52) Kashi, S.; Gupta, R. K.; Baum, T.; Kao, N.; Bhattacharya, S. N. Morphology, Electromagnetic Properties and Electromagnetic Interference Shielding Performance of Poly Lactide/Graphene Nanoplatelet Nanocomposites. *Mater. Des.* **2016**, *95*, 119−126.
(53) Rao, B. B.; Yadav, P.; Aepuru, R.; Panda, H.; Ogale, S.; Kale, S. Single-Layer Graphene-Assembled 3D Porous Carbon Composites with PVA and Fe_3O_4 Nano-Fillers: An Interface-Mediated Superior Dielectric and EMI Shielding Performance. *Phys. Chem. Chem. Phys.* **2015**, *17*, 18353−18363.
(54) Xu, P.; Han, X.; Wang, C.; Zhao, H.; Wang, J.; Wang, X.; Zhang, B. Synthesis of Electromagnetic Functionalized Barium Ferrite Nanoparticles Embedded in Polypyrrole. *J. Phys. Chem. B* **2008**, *112*, 2775−2781.
(55) Zakiyan, S. E.; Azizi, H.; Ghasemi, I. Influence of Chain Mobility on Rheological, Dielectric and Electromagnetic Interference Shielding Properties of Poly Methyl-Methacrylate Composites Filled with Graphene and Carbon Nanotube. *Compos. Sci. Technol.* **2017**, *142*, 10−19.
(56) Zhang, Z.; Dang, W.; Dong, C.; Chen, G.; Wang, Y.; Guan, H. Facile Synthesis of Core−Shell Carbon Nanotubes@ MnOOH Nanocomposites with Remarkable Dielectric Loss and Electromagnetic Shielding Properties. *RSC Adv.* **2016**, *6*, 90002−90009.
(57) Song, W.-L.; Guan, X.-T.; Fan, L.-Z.; Cao, W.-Q.; Wang, C.-Y.; Zhao, Q.-L.; Cao, M.-S. Magnetic and Conductive Graphene Papers Toward Thin Layers of Effective Electromagnetic Shielding. *J. Mater. Chem. A* **2015**, *3*, 2097−2107.
(58) Verma, M.; Singh, A. P.; Sambyal, P.; Singh, B. P.; Dhawan, S. K.; Choudhary, V. Barium Ferrite Decorated Reduced Graphene Oxide Nanocomposite for Effective Electromagnetic Interference Shielding. *Phys. Chem. Chem. Phys.* **2015**, *17*, 1610−1618.
(59) Tripathi, P.; Prakash Patel, C. R.; Dixit, A.; Singh, A. P.; Kumar, P.; Shaz, M. A.; Srivastava, R.; Gupta, G.; Dhawan, S. K.; Gupta, B. K.; Srivastava, O. N. High Yield Synthesis of Electrolyte Heating Assisted Electrochemically Exfoliated Graphene for Electromagnetic Interference Shielding Applications. *RSC Adv.* **2015**, *5*, 19074−19081.
(60) Geraldo, D. A.; Togo, C. A.; Limson, J.; Nyokong, T. Electrooxidation of Hydrazine Catalyzed by Noncovalently Functionalized Single-Walled Carbon Nanotubes with CoPc. *Electrochim. Acta* **2008**, *53*, 8051−8057.
(61) Ibrahim, A. A.; Dar, G.; Zaidi, S. A.; Umar, A.; Abaker, M.; Bouzid, H.; Baskoutas, S. Growth and Properties of Ag-Doped ZnO Nanoflowers for Highly Sensitive Phenyl Hydrazine Chemical Sensor Application. *Talanta* **2012**, *93*, 257−263.
(62) Dar, G.; Umar, A.; Zaidi, S.; Ibrahim, A. A.; Abaker, M.; Baskoutas, S.; Al-Assiri, M. Ce-Doped ZnO Nanorods for the Detection of Hazardous Chemical. *Sens. Actuators, B* **2012**, *173*, 72−78.
(63) Zaidi, S. A. Molecular Imprinting Polymers and their Composites: A Promising Material for Diverse Applications. *Biomater. Sci.* **2017**, *5*, 388−402.
(64) Seo, E. T.; Nelson, R. F.; Fritsch, J. M.; Marcoux, L. S.; Leedy, D. W.; Adams, R. N. Anodic Oxidation Pathways of Aromatic Amines. Electrochemical and Electron Paramagnetic Resonance Studies. *J. Am. Chem. Soc.* **1966**, *88*, 3498−3503.

DOI: 10.1021/acsami.7b05021
ACS Appl. Mater. Interfaces 2017, 9, 24179−24189